



Study on the spectral characteristics of IF signals and its influence on the performance of heterodyne Φ -OTDR

CHI ZHANG,^{1,2} CHENGZHEN LUO,^{1,2} XIYUAN ZHANG,³
SHAOXIONG TANG,^{1,2} CHENYANG DING,^{1,2}
IMTIAZ NASEEB AWAN,^{1,2} SHUAI TONG,^{1,2}  HAO DING,^{1,2}
TIAN XIAO,^{1,2} NINGMU ZOU,^{2,4} YIXIN ZHANG,^{1,2,5}
AND XUPING ZHANG^{1,2,6}

¹ College of Engineering and Applied Sciences, Nanjing University, Nanjing 210023, China

² Key Laboratory of Intelligent Optical Sensing and Manipulation, Ministry of Education, Nanjing University, Nanjing 210093, China

³ Communication Engineering at Harbin Institute of Technology, Shenzhen 518055, China

⁴ School of Integrated Circuits, Nanjing University, Suzhou 215163, China

⁵ zyixin@nju.edu.cn

⁶ xpzhang@nju.edu.cn

Abstract: The heterodyne phase-sensitive optical time-domain reflectometer (Φ -OTDR) is one of the most popular distributed optical fiber sensing (DOFS) technologies due to its high sensitivity, wide frequency response bandwidth, large dynamic range, and resistance to electromagnetic interference. In the signal processing workflow, like the I/Q algorithm, digital filtering of intermediate frequency (IF) signals is unavoidable. This study combines the advantages of the scattering point superposition model and the phase-modulated signal model. Three methods for quasi-matched IF filters are proposed. A signal evaluation system combining Parseval signal-to-noise ratio (Pa-SNR), peak-to-peak value, and signal-to-noise ratio (SNR) is employed. For CIC-type IF filters, it is recommended to cascade no more than 3 low-tap filters. For the variant CIC filter, its demodulation rate is faster than that of the other two filters. But resulted in an SNR of 10 dB lower than the CIC filter, and 15 dB lower than FIR filters because of the asymmetry of IF signals we demonstrated. For FIR-type IF filters, we recommend that the passband cutoff frequency should be at least 2.43 times the reciprocal of the pulse width. This factor decreases with increasing pulse width and narrowing of the transition band, but should not be lower than 1.08. Additionally, it is important to note that within approximately 0.8 times the transition band range of the cutoff frequency, half of the demodulation performance may degrade due to the IF filter passband ripple characteristics.

© 2025 Optica Publishing Group under the terms of the [Optica Open Access Publishing Agreement](#)

1. Introduction

Phase-Sensitive Optical Time-Domain Reflectometry (Φ -OTDR) has become one of the most widely used techniques in Distributed Optical Fiber Sensing (DOFS) and remains a prominent research focus nowadays [1]. Φ -OTDR is a powerful method that enables fully distributed vibration sensing along the entire sensing fiber. It offers fast response, high sensitivity, multipoint detection, and strong resistance to electromagnetic interference [2]. These features have made it suitable for various applications, including structural health monitoring, intrusion detection, underwater acoustics, and seismic monitoring [3–7].

Technological advancements and market demand have recently driven the adoption of heterodyne detection Φ -OTDR. This method is preferred due to its high sensitivity, extensive dynamic range, and capability for qualitative and quantitative measurements [8]. For demodulating

vibration signals, analog or digital filtering operations are essential [9–11]. Since the heterodyne beat frequency signal has an intermediate frequency (IF) carrier, this manuscript refers to it as the “IF signal”. Compared to analog filters, digital filters offer advantages such as programmability, stability, precision, resistance to interference, and ease of implementation, which is better suited to handle variations in IF signal characteristics caused by differences in the bandwidth and performance of optical and electronic components. Thus, designing a flexible digital filter with appropriate frequency response characteristics is critically important.

The frequency response characteristics of the IF filter are defined by its passband cutoff frequency, transition bandwidth, and stopband suppression ratio. Traditionally, researchers prefer to align the passband cutoff frequency with the minimum bandwidth of system components or the inverse of the pulse width [12,13]. Transition bandwidth and stopband suppression ratio are often determined empirically [14]. While these methods have scientific merit, they may result in suboptimal parameter settings, such as retaining excessive additive noise or overly suppressing practical vibration signal components [15]. Analyzing the IF signal properties and mechanism in Φ -OTDR is essential to designing an IF filter that better fits the signal, and this entails analyzing the noise levels, phase modulation data, and carrier signal.

The modeling of IF signals follows two approaches: The first method simplifies the IF signal as an ideal phase-modulated (PM) signal in communication [13,16]. This method clarifies the relationship between vibration and the phase variation of the IF signal, thereby elucidating the principle of heterodyne detection in Φ -OTDR demodulation. The model has a faster construction speed and can directly map the disturbances on the fiber under test (FUT) onto the PM carrier signal. At the same time, controllable fading regions can be set by adjusting the value of PM amplitude. However, it overlooks the random fluctuations in light intensity and phase caused by the inhomogeneity of the optical fiber during the scattering process, and it also fails to capture the impact of varying pulse light intensities injected into the fiber. Moreover, while the established distribution of fading regions does not significantly affect the analysis of fading noise in most cases, the probability distribution is unreasonable. The PM signal has an adequate bandwidth of twice the max phase modulation value, and about 98% of the energy is concentrated within a bandwidth [17,18]. The spectral characteristics of PM signals are usually determined by Bessel functions of the first kind. However, no relevant parameters of the pulse light, so the influence of the injected light on the demodulation cannot be represented.

The second modeling method references the Rayleigh backscattering (RBS) of waves in radar systems, establishing a physical model of the optical field by incorporating the random scattering of pulsed light in optical fibers [19–21]. This approach describes the light intensity of the received RBS and serves as the theoretical foundation for amplitude detection-based demodulation [22]. Based on multipath effects in radar, scattering sites in optical fibers are handled as a system function of the FUT. Initially, this method explored amplitude detection principles in Φ -OTDR systems [23,24]. Recent research has expanded its application to the analysis of optical phase variations. For instance, in 2017, a modular simulation model evaluated the effects of parameters such as laser linewidth, pulse width, and disturbance frequency on system response [25]. In 2018, the quality of amplitude detection was linked to phase demodulation reliability [17,26]. In 2020, a simplified model simulated static environmental changes in Φ -OTDR systems by treating the fiber as a one-dimensional waveguide with refractive index changes representing fiber stretching [27]. In 2024, a high-fidelity model was introduced, incorporating factors like coherent fading, polarization fading, laser frequency drift, and white noise, creating a simulation with adjustable parameters [28]. While the second method provides significant insights, it also has limitations. The random superposition of scatter points complicates observation of the central peak and sidelobes of the IF signal spectrum, and fading regions remain uncontrollable, potentially affecting vibration detection locations.

This manuscript combines elements of both modeling approaches to address these challenges and propose a theoretical model which offers a reliable evaluation framework and a general design concept for the IF filter. It provides precise modeling of IF signal characteristics, to facilitate the performance validation of various digital filter applications, thereby avoiding performance limitations caused by improper filter parameters. Additionally, the research findings offer guidance for selecting the most effective digital signal processing methods and assist in selecting components with optimal bandwidth and redundancy.

2. Theoretical analysis

2.1. Model of IF signal

Figure 1(a) illustrates a typical setup of the heterodyne Φ -OTDR system. A laser beam emitted by a laser source with a central frequency of F_0 is split by coupler1 into forward light and local oscillator (LO) light. The forward light is modulated by the AOM to produce a frequency shift of F_p , and at the same time, it is chopped into pulsed light, amplified by an erbium-doped fiber amplifier (EDFA), and injected into the FUT for scattering. The scattered light and the LO light, produce a beat frequency signal detected by a balanced photodetector (BPD). A data acquisition (DAQ) system digitizes the resulting electrical signal, sampled at a rate F_s , and converted into an IF signal via an analog-to-digital converter (ADC).

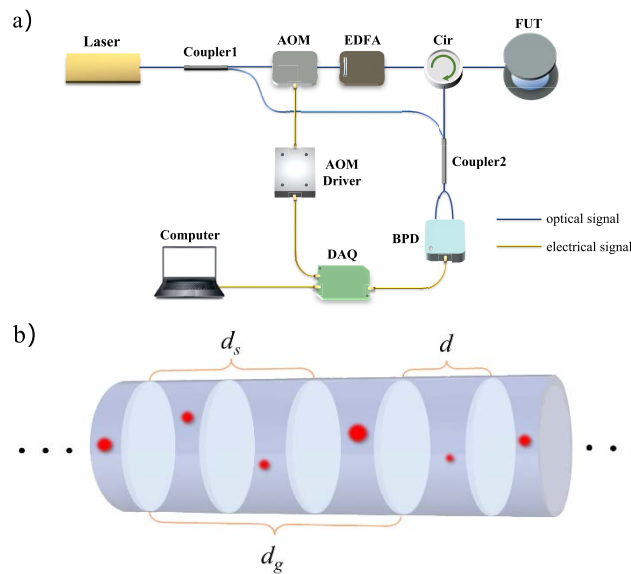


Fig. 1. (a) Schematic diagram of a typical coherent Φ -OTDR System. (b) The scattering point model of FUT.

Figure 1(b) shows the fiber is divided into N intervals, each represented by a single scattering center aggregating all scatterers within that interval. In the heterodyne Φ -OTDR, since the light injected into the FUT is a pulse of width W , and corresponding RBS light from the scattering point returns continuously. This is equivalent to detecting the superimposed scattered light from all scattering points within a gauge length $d_g = c \cdot W / (2 \cdot n_{ave})$ [28,29], where c is the speed of light, n_{ave} is the nominal refractive index of the FUT. This expression holds regardless of errors caused by the fiber fabrication [30]. Simultaneously, the ADC limits the spacing $d_s = c / (2F_s \cdot n_{ave})$. The larger one of d_s and d_g determines the minimum spatial resolution of the system. Theoretically, the spacing between scattering points in the FUT is much

smaller than the wavelength of the probe light [31], resulting in a vast number of scattering points. To balance computational cost and accuracy in numerical simulations, the scattering point density can be reduced while preserving model fidelity, achieving an equivalent scattering point interval d [32]. The interfered RBS light can be expressed as follows [25,31]:

$$E_R(t) = AE_0 \sum_{i=1}^N r_i \exp(-2\alpha L_i) \text{rect}\left(\frac{t - \tau_i}{W}\right) \exp(j\delta(\tau_i)). \quad (1)$$

where E_0 is the intensity of pulsed light. The refractive index of the i -th scattering point n_i determines the scattering coefficient $r_i = (n_i - n_{i+1})/(n_i + n_{i+1})$ [27]. $L_i = i * d$ is the distance from the start to the i -th backscattering point. α is the average loss coefficient of the fiber. $\tau_i = \tau_{i-1} + 2n'_i(L_i - L_{i-1})/c$ is the time required for the RBS light of i -th scattering point to return the circulator. In order to simplify the calculation of Eq. (1), we simplify the optical path changes caused by fiber strain, photoelastic effects, and the Poisson effect into variations in the refractive index n'_i of the disturbed fiber. At the same time, we focus on the response of Φ -OTDR to dynamic strain. Therefore, the strain caused by temperature change is ignored, and the equivalent index change induced by strain is $\Delta n_\varepsilon = n_{ave}(1 - 0.1n^2_{ave}) * \varepsilon$ [27]. The phase of i -th backscattering point $\delta(\tau_i) = 2\pi(F_o + F_p) * \tau_i + \theta_c$. Since the attenuation within a single pulse is negligible and can be disregarded, Eq. (1) can be simplified as [21]:

$$E_R(t) = \exp(-2\alpha L_t) AE_0 \sum_{i=1}^N r_i \text{rect}\left(\frac{t - \tau_i}{W}\right) \exp(j\delta(\tau_i)) = |B(t)| \exp(j\varphi(t)) \quad (2)$$

$$B^2(t) = \left\{ \alpha_t AE_0 \sum_{i=1}^N r_i \text{rect}\left(\frac{t - \tau_i}{W}\right) \sin(\delta(\tau_i)) \right\}^2 + \left\{ \alpha_t AE_0 \sum_{i=1}^N r_i \text{rect}\left(\frac{t - \tau_i}{W}\right) \cos(\delta(\tau_i)) \right\}^2 \quad (3)$$

$$\phi(t) = \tan^{-1} \left(\frac{\alpha_t AE_0 \sum_{i=1}^N r_i \text{rect}\left(\frac{t - \tau_i}{W}\right) \sin(\delta(\tau_i))}{\alpha_t AE_0 \sum_{i=1}^N r_i \text{rect}\left(\frac{t - \tau_i}{W}\right) \cos(\delta(\tau_i))} \right) \quad (4)$$

$\phi(t)$ not only represents the phase shift brought about by the modulation of the AOM, but also contains disturbance information from various positions along the optical fiber. LO light after splitting by coupler1 is $E_{LO}(t) = (1 - A) * E_0 * \exp(j\varphi_0(t))$, where $\varphi_0(t) = 2\pi F_0 t$. After interference of the LO light with the backscattering light, the output of a BPD with gain factor R can be expressed as [33,34]:

$$I_{out}(t) = R \left\{ \begin{array}{l} \frac{1}{\sqrt{2}} \left(E_R(t) + E_{LO}(t) \cdot e^{j\frac{\pi}{2}} \right) \cdot \frac{1}{\sqrt{2}} \left(\overline{E_R(t)} + \overline{E_{LO}(t)} \cdot e^{-j\frac{\pi}{2}} \right) \\ - \frac{1}{\sqrt{2}} \left(E_{LO}(t) + E_R(t) \cdot e^{j\frac{\pi}{2}} \right) \cdot \frac{1}{\sqrt{2}} \left(\overline{E_{LO}(t)} + \overline{E_R(t)} \cdot e^{-j\frac{\pi}{2}} \right) \end{array} \right\} \quad (5)$$

$$= 2R|B(t)|(1 - A)E_0 \cdot \cos\left(\phi(t) - \varphi_0(t) - \frac{\pi}{2}\right) + W_n(t)$$

The term $\varphi_0(t)$ does not include the laser frequency drift. This is because in heterodyne detection systems, the use of highly coherent light sources and phase difference in the spatial domain makes the drift reasonable to be ignored [35]. The thermal noise from all the other active devices is modeled as white noise $W_n(t)$. Since the superposition of scattering points and the amplitude of the IF signal white noise, both follow Gaussian distribution. The control of the signal-to-noise (SNR) level is achieved by managing the ratio of the standard deviation of $B(t)$ to that of $W_n(t)$, defining the logarithm of ten times this ratio as the IF carrier-to-noise ratio (IF-CNR), hereinafter referred to as CNR. It is worth noting that the simplified aspects of the

model are not irreversible; additional variables can be incorporated at appropriate locations to account for different influences. The reason why we ignored these factors such as environmental noise or polarization fading is that we are more concerned about the spectral characteristics of the IF signals during the process of coherent cancellation due to the superposition of scattering points. If too many variables are introduced, the system will become overly complex, and our simulation results will lose their representativeness.

2.2. Spectrum analysis of IF signals

Equation (5) gives the IF signal time-domain expression, allowing us to observe its spectrum characteristics through the Fourier transform. However, the random superposition of scattered light complicates the observation of elements such as the primary and side lobes and the bandwidth of the unnoisy signal. Simplified models are, therefore, necessary to evaluate spectrum properties effectively. One such model treats the IF signal as a typical PM signal detected by the BPD [17,36]:

$$U(t) = A(t)\cos((\pi F_p t + \varphi(t)) + W_n(t)). \quad (6)$$

The PSD of $U(t)$ is depicted by the orange in Fig. 2(a).

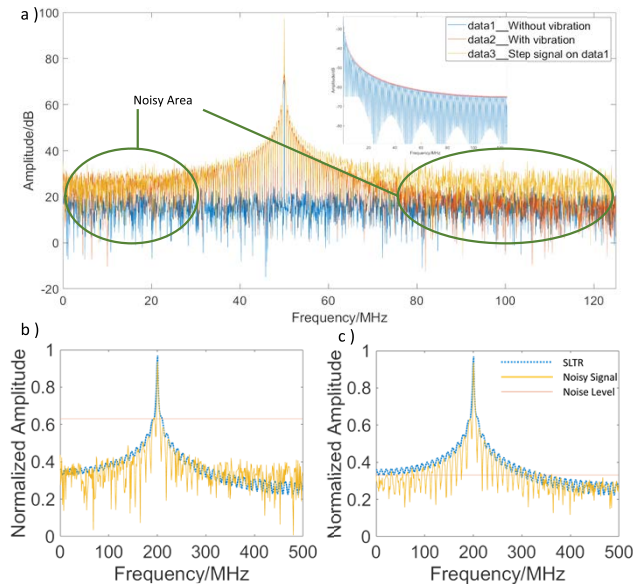


Fig. 2. In the simplified model of the IF signal, (a) a step signal is used to modulate the carrier signal, simulating phase modulation to numerically approximate its SLTR. (b) Noise level assessment by CNR = 12 (c) CNR = 18 dB. 8-bit ADC full-scale signal and quantization noise CNR is nearly 18 dB.

The curve shows a main lobe centered at the carrier frequency F_p with several side lobes, where the amplitude of adjacent side lobes gradually decreases. The region where the side lobe pattern periodically diminished is identified as the noise region. The zeros and amplitudes of Bessel function theoretically determine the amplitude characteristics of PM signal. By giving the modulation depth of the signal $\varphi(t)$, the coefficients of the Bessel function can be determined, which in turn defines the spectrum characteristics of the PM signal. However, the time for the pulsed light to travel through the FUT is often much shorter than the pulse interval time.

Therefore, $U(t)$ can be expressed as [27]:

$$U(t) = \begin{cases} U(t) = A(t)\cos(2\pi F_p t) + W_n(t) & t \leq t_s \\ U(t) = A(t)\cos(2\pi F_p t + \varphi_k) + W_n(t) & t > t_s \end{cases}. \quad (7)$$

t_s is the time for light to travel from the start to the disturbed location in FUT. φ_k is the phase change caused by the disturbance on the FUT of the k -th pulse of light. Equation (7) indicates that Bessel functions are unsuitable for describing the IF signal observed in the Φ -OTDR system. This is because the phase resulting from the scattering of a single pulsed light no longer presents as a continuously varying modulation, but rather exhibits the characteristic of discontinuous abrupt changes at the disturbed points. Thus, step signals with finite length multiplied on the carrier can be used to present the spectral characteristics of a PM signal. As the yellow curve shown in Fig. 2(a), the IF signal without phase modulation multiplied by the step signal is almost identical to the PM signal in terms of main lobe width and side lobe number of the spectrum, etc. It is feasible that deducing the attenuation rate of IF signal spectral sidelobe to researching the extension characteristics of IF signal according to the discrete Fourier transform expression of step signal $X(f)$:

$$X(f) = \sum_{i=1}^{t_1} A_1 \exp\left(-\frac{j2\pi fi}{N}\right) + \sum_{i=t_1+1}^{t_2} A_2 \exp\left(-\frac{j2\pi fi}{N}\right). \quad (8)$$

Here, A_1 and A_2 , represent the amplitudes before and after the vibration point of the step signal, respectively. Multi-step signals can also be employed to simulate phase modulation at multiple locations along the FUT. This method is beneficial for mathematically deriving the sidelobe attenuation rate (SLTR) of IF signals, enabling the distinction between the bandwidth occupied by noise and that of the effective signal.

According to Parseval theorem, which states that energy is conserved in both the time and frequency domains, it is possible to plot the noise level threshold line based on the CNR in the spectrum. The intersection of this threshold line with the SLTR curve determines the bandwidth of the noise-influenced region, as illustrated in Fig. 2(b) and (c). It should be noted that this kind of simulation is applicable to scenarios where the interference in the optical fiber link is relatively small and singular. Under complex interference conditions, it is rather difficult to set the amplitude of the step signal, which may introduce obvious errors. While using a step signal may introduce some potential noise level evaluation errors, this approach remains an effective and rapid method for assessing the quality and bandwidth of IF signals.

2.3. Quasi-matched IF filter design

The ideal approach to filter designing is to establish a matched IF filter based on the system function of the IF signal [37]. The impulse response of the matched IF filter is set to the time-reversal and complex conjugate of the IF signal, ensuring that the passband and stopband shapes of the filter are entirely consistent with the spectrum characteristics of the IF signal. This matched filter can then be convolved with the IF signal to combat white noise and extract the IF signal with maximum SNR. At low CNR, the contribution of fading noise significantly increases comparing to white noise [38,39]. Therefore, the IF signal will focus on not being overwhelmed by excessive white noise. The inability of traditional matched filters to effectively match non-deterministic signals and suppress non-white noise is a significant drawback. Utilizing the concepts of matched filters, we suggest the design of a quasi-matched intermediate frequency filter, emphasizing the selection of passband cut-off frequency, transition bandwidth, and stopband suppression ratio.

The time-domain response of digital filters may cause the spectrum of the IF signals to experience superposition and smearing. Therefore, it is essential to ensure that after the IF signal passes through the filter, the spatial resolution of the demodulated result does not fall below the minimum spatial resolution. Usually, the passband width of the quasi-matched IF filter should be optimized on the base of the inverse of pulse width $1/W$ [40]. Incidentally, since the rising edge of AOM proved to be narrow, the impact of the steepness of the rising edge on modeling is not concerned.

Finite impulse response (FIR) filters exhibit high stability, linear phase response, flexible magnitude response and anti-aliasing. Typically, a FIR filter with D orders, the transfer function of which is given by:

$$H(Z) = \sum_{k=0}^D h(k)Z^{-k}. \quad (9)$$

We define the number of points that account for 90 percent of the energy as the spatial aliasing degree (SAD) caused by this FIR filter. This value should be comparable to the spatial resolution of the system. However, in some cases, FIR filters require more taps to achieve the steep transition band or high stopband suppression ratio, which generates significant overall signal delay, leading to the reduction of effective measurement length.

A cascaded integrator-comb (CIC) filter is one type of special FIR filter as a matched filter of pulse waveform in the communication system. Whether the CIC filter is the best match in Φ -OTDR must be verified. On one hand, under the same passband bandwidth, the CIC filter requires fewer taps which degradation signal delay. On the other hand, drooping in the passband and leakage in the stopband could deteriorate the SNR of the IF signal. The transfer function of the CIC filter applied to the down-converted I and Q paths in traditional IQ demodulation methods can be expressed as:

$$H(Z) = \frac{1}{D} \sum_{k=0}^{D-1} Z^{-k} = \frac{1 - Z^{-D}}{D(1 - Z^{-1})} = \frac{1 - e^{-jD\omega}}{D(1 - Z^{-1})}. \quad (10)$$

We propose a variant CIC filter for bandpass filtering of the I/Q path to optimize the rate of IQ demodulation operations [26]. Periodicity introduced into the tap coefficients $X_n = [X_1 \cdots X_m, X_1 \cdots X_m]$, and when D is an integer multiple of period m , the transfer function of the filter is given by:

$$\begin{aligned} H(Z) &= \sum_{k=0}^{D-1} X_k Z^{-k} = \frac{X_1(1 - Z^{-D}) + \cdots + X_m(1 - Z^{-D-m+1})}{1 - Z^{-m}} \\ &= \frac{(1 - Z^{-D})(X_1 + X_2 Z^{-1} + \cdots + X_m Z^{-m+1})}{1 - Z^{-m}}. \end{aligned} \quad (11)$$

By calculating the poles of Eqs. (10) and (11), the passband centers for the two types of CIC filters can be obtained. The zero points adjacent to these poles, along with the passband center positions, indicate the passband bandwidth, which is inversely proportional to the filter order D . Since the digital implementation of CIC filters typically involves a sliding average, unlike FIR filters, a D -tap CIC filter results in the spatial resolution of system not being less than an equivalent spatial length of D sampling points.

2.4. Performance evaluation of phase demodulation

When evaluating the SNR of the Φ -OTDR system for a single-tone vibration signal, we typically calculate the ratio between the value at its characteristic frequency on the power spectral density (PSD) and the noise value in the high-frequency region away from the characteristic frequency

[26,41]. Using PSD allows intuitive observation of the proportion of different frequency components within a signal. When demodulating a monophonic vibration signal, if the noise region selected for calculating SNR is influenced by high-frequency noise interference or if harmonic energy contributes significantly, it may cause considerable fluctuations in SNR. This is primarily due to the lack of a quantitative measurement standard for selecting the noise region. We know from Parseval theorem [42] $\int |x(t)|^2 dt = \int |x(f)|^2 df$, that energy is conserved before and after Fourier transformation. The discretization expression is:

$$\sum_{i=1}^N x(t_i)^2 = \sum_{i=1}^N |X(f_i)|^2 / N. \tag{12}$$

$$\left[\frac{|X(f_1)|^2}{\sum_{i=1}^N x(t_i)^2 / N} + \frac{|X(f_2)|^2}{\sum_{i=1}^N x(t_i)^2 / N} + \dots + \frac{|X(f_N)|^2}{\sum_{i=1}^N x(t_i)^2 / N} \right] = 1. \tag{13}$$

Each term in Eq. (13) constitutes a normalized array whose sum is 1, which we define as Pasval-SNR (Pa-SNR). It helps us build a direct reflection of the energy of each frequency point as a percentage of the analyzed signal. As shown in Fig. 3, We simulated signals with several characteristic eigenfrequencies, just because the number of points involved in the simulation is

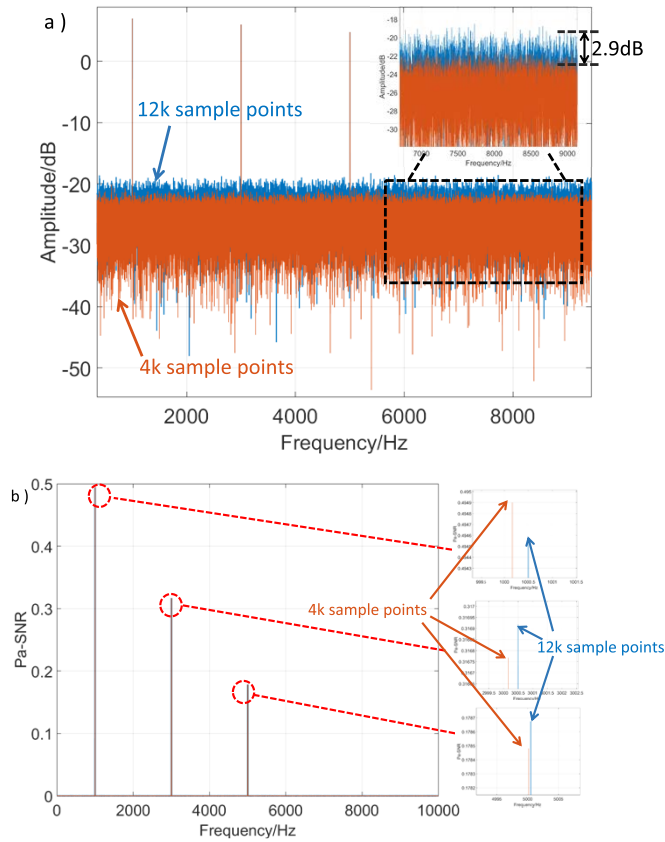


Fig. 3. Comparison of results from (a) traditional SNR assessment and (b) Pa-SNR assessment for two sets of signals with the same frequency but different lengths.

triple, the SNR difference between the two signals is about 2.39 dB, and the Pa-SNR differences are only about 0.0003. The characteristic frequency values are almost identical in the PSD, but the difference in the noise levels is relatively significant. The difference between SNR and Pa-SNR may reflect the same thing—the proportion of wide-spectrum white noise increases as the number of sampling points. However, the reliability of the two results shows a clear gap, and the 3 dB SNR difference cannot usually be ignored. Therefore, the selection of noise regions is crucial for the accuracy of SNR results. We should note that logarithmic processing is not applied to Pa-SNR. That means Pa-SNR is more suitable for analyzing signals with known characteristic frequencies, signals with unknown frequencies are less visible. We use SNR, Pa-SNR, and the peak-to-peak (P-P) values of the demodulated vibration signals as standard criteria to evaluate the demodulation.

3. Simulation settings and verification

3.1. Simulation settings

According to the setup in Fig. 1(a), the simulation parameters of this manuscript are as follows. To achieve a narrower rising/falling edge while minimizing low-frequency noise, we choose the AOM frequency F_p to be 200 MHz. Consequently, to ensure an oversampling rate of four to five times, we set the ADC sampling frequency F_s to 1 GHz. Typically, when setting up a system, bandwidth-matched BPD and ADC are selected to minimize the acquisition of system noise by the ADC. In this simulation, we will remove the bandwidth constraints of the BPD and ADC to study the frequency spectrum characteristics of the IF signal over a broader frequency range. The average refractive index of the fiber is set to 1.5, and the splitting ratio of Coupler 1 is 1:9. Similarly, even if some component parameters are modified, the methods for configuring the heterodyne detection Φ -OTDR can still refer to the settings outlined here.

Before setting the pulse repetition frequency and vibration event parameters, we need to clarify the concept of modulation depth (MD) and maximum swing rate (MSR). Some researchers have studied the relationship between the vibration intensity or frequency applied to FUT and the demodulation accuracy [25]. We recognize the peak value of the applied sinusoidal vibration signal as MD, while its frequency, along with the pulse repetition frequency of system, constitutes the MSR $2 \sin \pi / f_s * f_p$. Due to the limitations of the phase unwrapping algorithm, if the phase difference between two adjacent sampling points exceeds $\pm\pi$, unwrapping will fail, leading to demodulation errors. When observing the vibrating region, the maximum phase difference occurs at the moments when two adjacent points are symmetrically distributed around the zero-crossing points of the sine wave. Specifically, unwrapping will fail when the MD and the sampling MSR product exceeds $\pm\pi$. Based on this foundation, we set the pulse repetition and the vibration intensity/frequency to avoid unwrapping failures. The pulse repetition frequency is set at 1000 Hz, with the frequency of vibration event A being 66.5 Hz and B being 129 Hz. This configuration distinguishes which event produces the harmonic signals and adjusts the vibration intensity. To avoid fading noise, we simulate the FUT length of about 100 meters, use a specific group of scattering light intensities as a baseline, and set the vibration events at 0.1 and 0.4 times the total length.

3.2. Simulation correctness verification

There has been considerable work on the reliability assessment of Φ -OTDR simulation models. We adopt some previously validated arguments to verify the accuracy of our model, ensuring that our conclusions are robust. Figure 4(a) shows the superposition of multiple cycles of the IF signal. Outline the characteristics of the FUT. It is observed that there are several coherent fading regions along the FUT. After outlining the FUT and without considering changes in the polarization state, the fading regions remain unchanged. At the same time, since the system synchronizes the

clock source of the AOM and ADC, there is no initial phase difference for each IF signal [38]. That is, cycles of the IF signal before the first vibration area overlap significantly, while there is an inevitable phase shift between each cycle after the vibration position. Figure 4(b) and (c) respectively demonstrate that the numerical distribution of the IF signal roughly conforms to a normal distribution and that $B^2(t)$ roughly follows a Rayleigh distribution. Since this simulation does not suppress the fading noise, a considerable portion of the values will be distributed near 0 [21,27]. Figure 4(d) shows the power spectral density (PSD) of the IF signal, where the main peak is observed at the center frequency. The side lobes become irregular due to the random superposition of scattering points, aligning with the actual characteristics of the signals captured by the ADC.

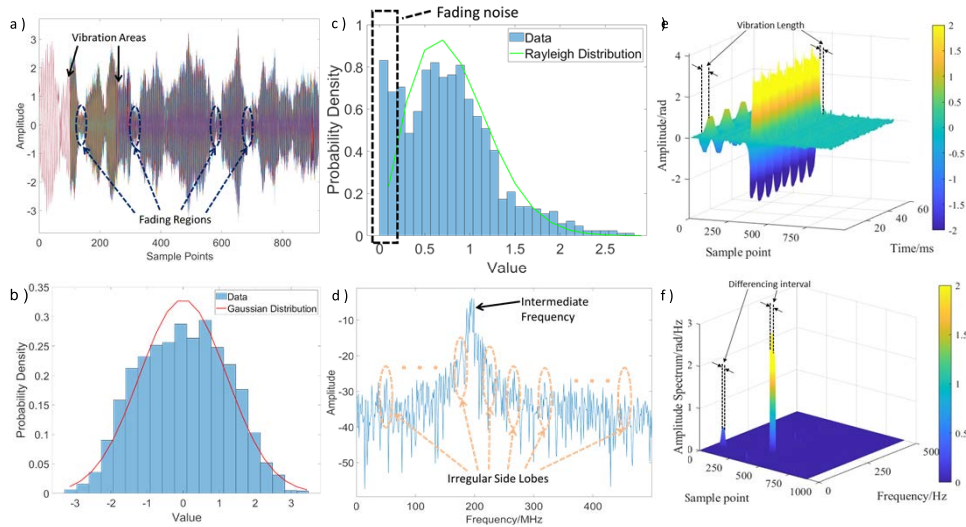


Fig. 4. Characteristics of simulated signals: (a) Several IF signals with applied vibration modulation, (b) Statistical probability distribution of the IF signals, (c) Statistical analysis of RBS energy, (d) PSD of the IF signal. (e) Time-space distribution of the demodulated phase., (f) Amplitude spectrum of the FUT.

After verifying the correctness of the time-domain and frequency-domain characteristics of the simulation signals, we further need to validate the correctness of the simulated vibration signals applied to the FUT. Figure 4(e) and (f) present the space-time signal and amplitude spectrum after phase demodulation, respectively. We observe that consistent with preset parameters, the single-tone vibration signals are located at 0.1 times and 0.4 times the total length of the FUT, with vibration lengths of 0.2 m and 0.1 m, respectively. The P-P ratio of the two vibration events aligns with the preset values. Additionally, the width of the vibration events corresponds to the differencing phase detection interval.

4. IF characteristics and filter design suggestions

In this section, we will apply different IF filters to the simulation data described in the previous section. Exploring whether the IF signal exhibits asymmetry, evaluating the performance of IF filters designed using various methods under different CNR and FUT vibrations. We will summarize the design principles and provide design guidelines for quasi-matched IF filters tailored to different scenarios. Qualitative conclusions presented in this section are not specific to the chosen parameter set, as similar results can be obtained with different parameter combinations;

thus, we do not elaborate on the rationale for this specific choice. Conversely, we will provide detailed explanations for the parameter selections for quantitative conclusions.

4.1. Asymmetry of the sidebands around the intermediate frequency

In communication systems, IF signals typically exhibit symmetry around the intermediate frequency. If the IF signals in the Φ -OTDR system also follow this rule, preserving the double-sideband signal could increase the proportion of the effective signal, thereby combating random additive noise. Otherwise, it would have the opposite effect. We processed IF signals at different CNR levels by multiplying them with the digital intrinsic signal and applying low-pass/band-pass FIR filters with the same transition bandwidth and stopband attenuation. The center frequency of band-pass filter coincided with the intermediate frequency of signal, and its bandwidth was double that of the low-pass filter, thus preserving the double-sideband signal. The results are shown in Fig. 5.

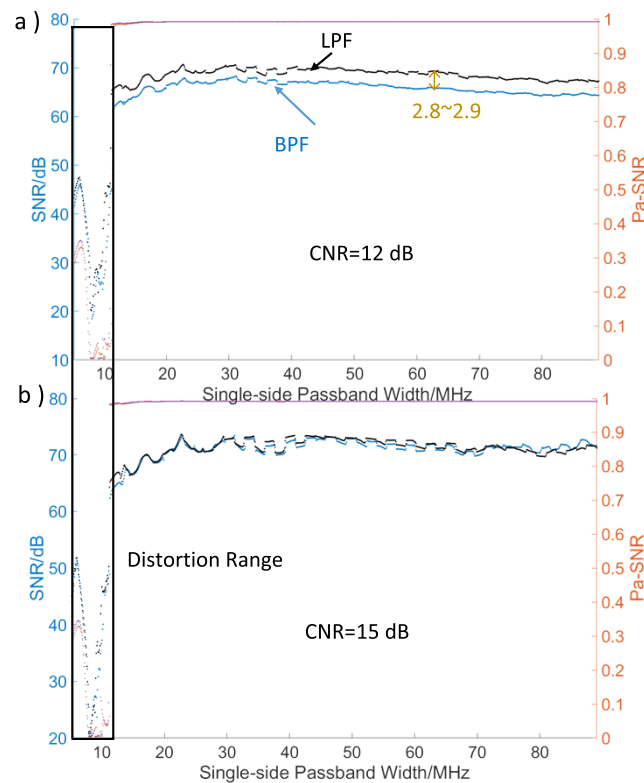


Fig. 5. At MD = 5, PW = 48 ns, comparison of the demodulation of vibration-modulated IF signals between (a) CNR of 12 dB and (b) CNR of 15 dB with retention of single sideband and both sidebands.

When the CNR = 12 dB, regardless of the variation in passband width, the SNR of the demodulated single-tone signal from the single-sideband IF signal is approximately 2.8 dB higher than that from the double-sideband signal, as for the formation of the distortion region shown in the figure, the subsequent part will explain. However, when CNR = 15 dB, the difference in SNR for the single-tone signals is negligible. This phenomenon indicates that in an Φ -OTDR system, as the noise level increases, the effective information carried by the double-sideband IF signal becomes more differentiated; thus, retaining the double-sideband fails to suppress white noise and may worsen the demodulation performance.

4.2. Performance evaluation of CIC type IF filter

Figure 6 compares the demodulation results using a bandpass CIC filter against a low-pass CIC filter, showing that the SNR of former is generally about 10 dB lower. This observation further corroborates the influence of IF signal asymmetry on the demodulation performance. Even the SNR of low-pass CIC filter results are 5 dB lower than the SNR of the FIR filter in Fig. 5. This is because of the lower stopband suppression ratio of the CIC filter compared to FIR filters, resulting in stopband leakage. The passband roll-off further suppresses the practical information of IF signal, amplifying the drawbacks of retaining the double sideband.

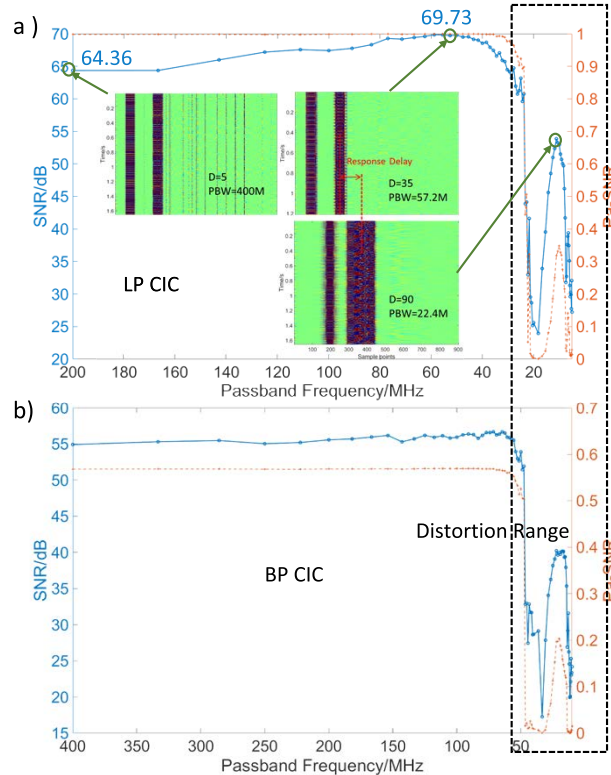


Fig. 6. At MD = 3, PW = 48 ns, CNR = 24 dB, comparison of the demodulation of vibration-modulated IF signals under (a) low-pass CIC filter and (b) band-pass filter with retention of single sideband and both sidebands.

Figure 6(a) shows the demodulation results for different settings of D . When $D = 5$, although the number of points involved in the convolution calculation is minimal, leading to the fastest computation speed and minimal impact on spatial resolution, the reduced number of points results in inadequate suppression of fading noise, causing numerous vertical stripes at quiet positions of the FUT. In contrast, with $D = 90$, there is an overlap between the two vibration signals and insufficient bandwidth to retain enough practical information, resulting in low SNR and Pa-SNR for the demodulated vibration signals and significant filter delay.

CIC filters can reduce stopband leakage through cascading while maintaining relatively low response delays. Figure 7 presents the demodulation results after cascading the low-pass CIC filter 2 and 3 times. Notable findings include that after 2 and 3 orders of filtering, the SNR of the single-tone signal improved by 1.84 dB and 2.44 dB, while the best demodulation results for the single-tone signal increased by 0.31 dB and 1.7 dB. Additionally, the range of distortion gradually

widened with the number of cascades, expanding by 5.8 MHz and 9.5 MHz, respectively. It was observed that cascading CIC filters effectively improve the quality of IF signal demodulation while the rate of increase in the distortion range diminishes. Cascading CIC filters effectively improve the quality of IF signal demodulation while the rate of increase in the distortion range diminishes.

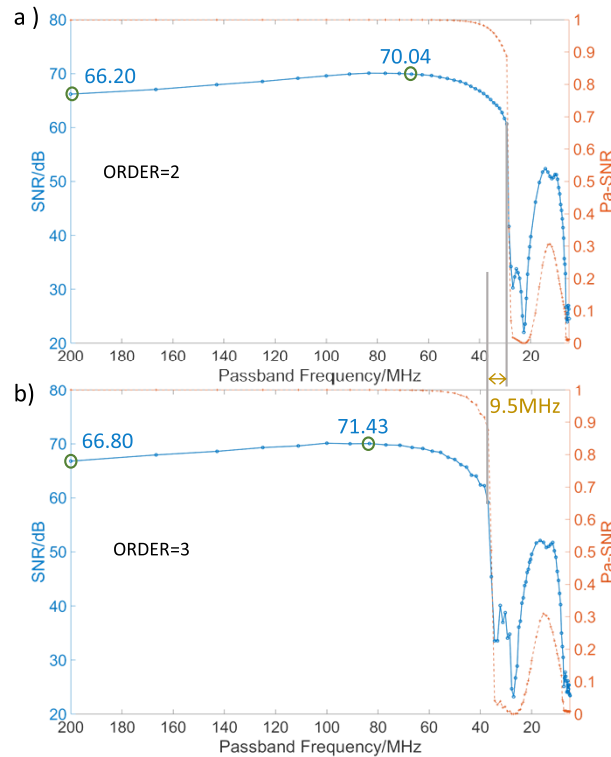


Fig. 7. At MD = 3, PW = 48 ns, CNR = 24, comparison of the demodulation of vibration-modulated IF signals under (a) 2-order low-pass CIC filter and (b) 3-order low-pass.

In summary, the CIC-type IF filter design could be flexible. The use of variant CIC filters in conjunction with rapid IQ algorithms can achieve the fastest demodulation rates, although the quality of signal demodulation may be lower than that achieved with low-pass CIC filters. By cascading CIC filters, the issue of stopband leakage can be effectively mitigated, resulting in better performance for IF signals. Therefore, we recommend that when designing general instrumentation of Φ -OTDR, considering hardware resource allocation, a bandpass CIC configuration with fewer taps combined with fast IQ algorithms will be the most efficient demodulation method. For cases requiring a balance between system computational efficiency and the SNR of the demodulated signal, a low-pass CIC filter may be used. For single-order low-pass CIC filters, the corresponding delay is linearly related to the filter order D . For multi-order low-pass CIC filters, it is advisable not to have too many stages. This is because CIC filters basically employ the moving average method, an excessive number of cascading times will cause signal aliasing and reduce the spatial resolution of the system. Moreover, the marginal benefit of the increase in the SNR brought about by cascading is significant, and the improvement of the system performance is limited compared with the increase in the cascading order. Also, attention should be paid to controlling the value of D to prevent distortion that may lead to signal demodulation errors.

4.3. Performance evaluation of FIR type IF filter

Figure 8(a) shows the demodulation results at position 1 when $\text{CNR} = 24$ dB, $\text{PW} = 48$ ns, and the transition bandwidth of the FIR-type IF filter is set to 4 MHz, with an increasing passband cutoff frequency. Several phenomena are noteworthy:

- (1) The bandwidth of the distortion region in Fig. 8 is narrower compared to Fig. 6 and Fig. 7. This is because when the passband bandwidth is close to $1/W$, the number of SAD points for the CIC type is higher, making it more susceptible to aliasing between different vibration signals.
- (2) The SNR results for the single-tone vibration signal at bandwidths of 11.0 MHz and 11.3 MHz are 49.96 dB and 63.26 dB. This seems to indicate a similar demodulation quality as shown in Fig. 6(b). However, the Pa-SNR results of less than 0.1 indicate a stronger contribution from harmonic components than a preset value. This could be proved by the distorted time-domain waveform at 11.0 MHz. And although the waveform at 11.3 MHz appears to have a good sinusoidal shape, its P-P value deviates significantly from the intended 2 rad. Therefore, incorporating Pa-SNR or P-P as auxiliary metrics for assessing signal demodulation quality is a more reliable approach.
- (3) As the passband cutoff frequency continues to increase, we observe fluctuations in the SNR curve with a period of approximately 3.3 MHz, and half of the SNR within one period about 2~3 dB lower than the other half. To investigate the cause of this phenomenon, we replicate the results of Fig. 8(a) using IF filters with a suppression ratio of 80 dB and transition bandwidths of 2/4/6/8/12/24 MHz. The periodic relationship is shown in Fig. 8(b), where it is observed that as the transition bandwidth increases, the periodicity with the ratio to the transition bandwidth around 0.8, gradually rises. This occurs because the filter tap is inversely proportional to the transition bandwidth. Additionally, the periodicity of the passband ripple is also inversely proportional to the filter tap. Since the energy of the down-converted IF signal is strongest near the 0 Hz frequency, the periodic variation of the passband ripple significantly influences the demodulation outcome. Therefore, the periodicity of the demodulation results is proportional to the ripple periodicity and transition bandwidth. Moreover, it is observed that when the transition band is narrow, the fluctuations in the SNR curve are more pronounced compared to when the transition band is wider. This is because the ripple level also increases with the filter tap, and its periodicity has a more significant impact on signals near 0 Hz.
- (4) Fig. 8(a) shows at 22.8 MHz, the demodulation result exhibits optimal performance for the first time, while $1/W$ is about 20.83 MHz. We define that point as the minimal non-distorted frequency of the IF filter. Using 6 sets of signals with PW ranging from 32 ns to 112 ns, with a step size of 16 ns, the minimal non-distorted frequency points for each set based on three-parameter-evaluation are plotted in Fig. 8(c). Narrower the transition band of the IF filter, the first non-distorted frequency point is closer to $1/W$ when the PW is the same. When the PW varies, the curve becomes more linear. This demonstrates that, the side lobe components increasingly contribute to the signal as the transition bandwidth increases, leading to higher instability in the demodulation results.

According to the aforementioned four conclusions, the FIR-type IF filter should target a narrower transition band, provided that the SAD impact does not exceed the spatial resolution of system. As long as the selected passband cutoff frequency circumvents the low SNR zone, a smaller initial non-distorted frequency signifies a broader array of options for the passband cutoff frequency. This also indicates that the bandwidth selection range of system components is broader. Conversely, a narrower component bandwidth may provide a greater SAD in return for

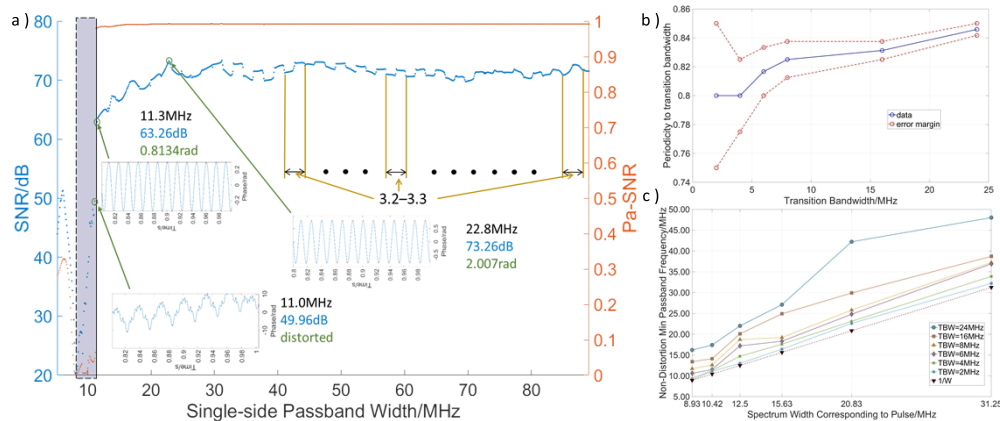


Fig. 8. Assessment of demodulation effectiveness of sinusoidal vibration signals as the bandwidth of FIR IF filter continuously changes. (a) SNR and Pa-SNR results with 0.1 MHz step, time domain plots at some nodes are shown (b) Periodicity to different transition bandwidths (c) Non-distortion Minimum passband frequency

enhanced demodulation performance. This research does not concentrate on noise suppression in low CNR situations; however, the results depicted in Fig. 8 pertain to $\text{CNR} = 24$ dB. Nonetheless, according to Fig. 2, it can be deduced that at low CNR, a more significant number of frequency components of the IF signal are obscured by noise. The selection range for the passband cutoff frequency to provide optimal demodulation performance will be reduced, necessitating a narrower transition band for the IF filter.

4.4. Effects of vibration signal modulation

A previous study mentioned that when the frequency of the single-tone vibration applied to the FUT remains constant, the larger the vibration intensity, the greater the demodulation deviation. Conversely, when the vibration intensity is fixed, lower frequencies lead to smaller demodulation deviations, showing a linear relationship [25]. We have verified the correctness of this conclusion. In a heterodyne Φ -OTDR system, the validity of this conclusion depends on the condition outlined in Section II: the MD and MSR product must not exceed π , ensuring that phase unwrapping does not fail. Figure 9 shows that demodulation failure is probable when the combination of MD and MSR approaches π but has not yet reached the theoretical limit. As the vibration intensity increases and approaches the critical value, significant deterioration in signal demodulation can occur.

In Fig. 9(c), where MD is 3 and f_p is 66.5 Hz thus MSR is 0.415, the probability of demodulation entering the distortion region is lower compared to Fig. 9(d), where MD is 3.5 and f_p is 129 Hz thus MSR is 0.789, even though the latter has a larger MD and MSR product. This confirms that lower frequencies improve demodulation performance, especially as the MD and MSR product approaches its theoretical limit. Therefore, when the monitored signal approaching the theoretical limit, selecting an appropriate IF filter is key to accurate demodulation.

4.5. Discussion

Our model emphasizes reproducing the pulse light energy and the process of random scattering point superposition, which inevitably introduces random fading noise. We avoid fading by generating multiple sets of scattered light signals continuously and selecting those scattered light signals from the preset vibration region of the FUT that are unaffected by fading noise as templates. These templates are then used to generate IF signals under various parameters. The

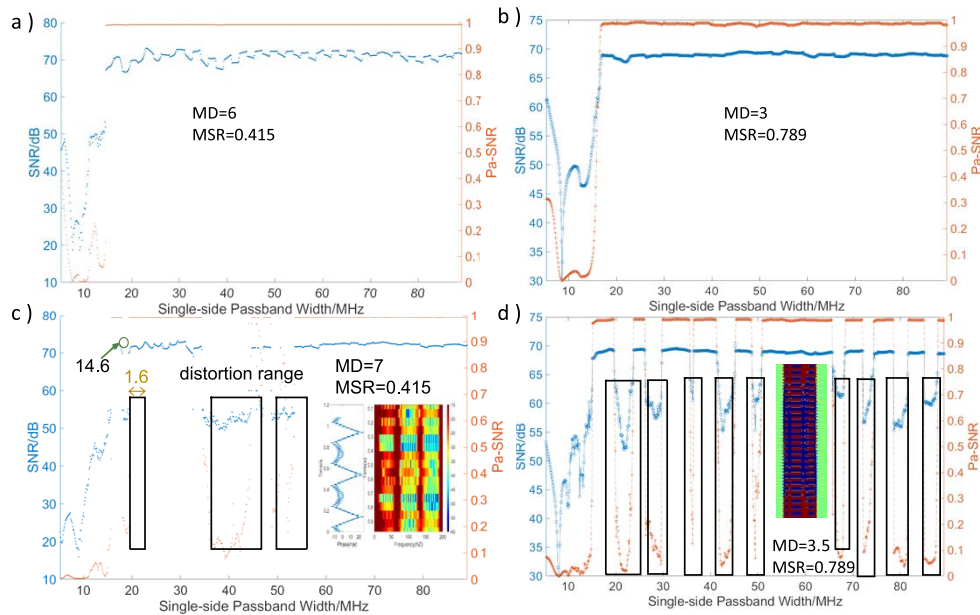


Fig. 9. Different filter widths on demodulation at different MD and MSR.

model construction is extended to the BPD output results, rather than replacing it with PM signals. At the same time, we have established a simplified noise evaluation model based on PM signals to roughly assess the proportion of noise in the IF signal spectrum under different CNR levels.

We evaluate the demodulation performance of single-tone vibration signals to infer specific characteristics of the IF signals and assess the advantages and disadvantages of different filter design methods. SNR, Pa-SNR, and P-P are evaluation factors, and the demodulation performance is assessed from three aspects: the power-frequency distribution of the vibration signal, frequency tonal consistency, and time-domain stability. We first verified that the IF signals exhibit asymmetry, which leads to higher asymmetric noise when applying a variant CIC filter. Although applying variant CIC filters achieved high computational rates, it introduced more significant asymmetric noise, particularly when the CNR is low. Although CIC-type IF filters can improve demodulation performance through cascading, our study suggests that cascading should generally not exceed three orders, with two orders being optimal. For FIR-type IF filters, we observed that the demodulation results exhibit periodic behavior as the passband cutoff frequency changes, confirming the hypothesis that the period is related to the transition bandwidth.

Furthermore, we established the relationship between the first non-distorted demodulation frequency point and the pulse bandwidth, along with the transition bandwidth of the filter, under different pulse width settings. The narrower the pulse bandwidth and the transition bandwidth, the closer the first non-distorted demodulation point approaches the pulse bandwidth. As shown in Table 1, we give a series of suggestions about IF filter selection and design. This table is more inclined to describe the relative relationship between several filtering methods. Therefore, we define the evaluation result of a specific filter as the reference value of 1. For the other two, if their values are dimensionless, they are related to the reference value by a multiplicative factor. If their values have dimensions, the relationship is expressed in terms of relative addition or subtraction. The absence of units in the table indicates that we have adopted a dimensionless evaluation. At the same time, the values given in the table are approximate estimates obtained under normal scenarios, not under extreme settings.

Table 1. Difference between various IF filters

	Variant CIC	CIC	FIR	Remarks
Demodulation speed	>60	>30	1	greater difference by longer the FUT or bigger F_s or smaller W
Memory usage	1	>2	>2.5	greater difference by longer the FUT or bigger F_s
Demodulation tonal of vibration	1 dB	>5 dB	>15 dB	greater difference by lower CNR
Big vibration demodulation distortion rate	>3	>1.5	1	greater difference by lower CNR or bigger MSR, MD
Double-sideband demodulation SNR deterioration	>5 dB	>3 dB	1 dB	greater difference by lower CNR
Response delay	1	>2	>30	greater difference by bigger F_s/F_p or smaller W
Suitable cascades orders	2~3	2~3	1	for CIC type, lower taps filter can tolerate more orders. And no cascaded need for FIR-type
Scope of application	Online demodulation Low hardware cost High CNR Low system dynamic range Short FUT	A compromised solution	Offline demodulation High hardware cost Low CNR High system dynamic range Long FUT	Design considerations in suitable scope: For CIC types, a low D ensures passband cut-off frequency away from the deterioration range. For FIR type, a high D ensures narrow transition bandwidth, note the periodicity of the passband ripple, passband cut-off frequency close to the first non-deterioration range.

The methods and results described in this manuscript are not comprehensive enough, as some aspects still have not been fully considered. For example, during the modeling and simulation, we did not open all the parameter interfaces to allow real-time matching with the system components. Additionally, the design of the IF filter, such as the selection of parameters like stopband attenuation and window functions, was limited in terms of combinations, and the types of applied vibration signals were relatively simple. In future work, we hope to combine AI models to conduct extensive parameter scanning, providing more detailed conclusions and uncovering even more interesting scientific phenomena, to further “extract” the performance limits of heterodyne Φ -OTDR.

5. Conclusion

This study combines the advantages of the scattering point superposition and PM signal models. Three methods for quasi-matched IF filters are proposed. An evaluation criterion that uses Pa-SNR and peak-to-peak to assist in SNR assessment. CIC-type IF filters are recommended to cascade no more than three low-tap filters. Using a variant CIC filter achieved one order of magnitude faster demodulation speed. However, because of our demonstrated asymmetry of IF signals, it resulted in an SNR of 10 dB lower than the CIC filter and 15 dB lower than FIR filters. For FIR-type IF filters, we recommend that the passband cutoff frequency should be at least 2.43

times the reciprocal of the pulse width. This factor decreases with increasing pulse width and narrowing of the transition band, but should not be lower than 1.08. Additionally, it is important to note that within approximately 0.8 times the transition band range of the cutoff frequency, half of the demodulation performance may degrade due to the IF filter passband ripple characteristics. When the MSR and MD settings approach the limit, examining whether unwrapping failure occurs due to improper filter settings is necessary.

Funding. National Natural Science Foundation of China (62175100); Fundamental Research Funds for the Central Universities (2024300447, 0213-14380264, 0213-14380265).

Disclosures. The authors declare no conflicts of interest.

Data availability. Data underlying the results presented in this manuscript are not publicly available at this time but may be obtained from the authors upon reasonable request.

References

1. Y. Rao, Z. Wang, H. Wu, *et al.*, “Recent advances in phase-sensitive optical time domain reflectometry (Φ -OTDR),” *Photonic Sens.* **11**(1), 1–30 (2021).
2. M. Soriano-Amat, H. F. Martins, S. Martin-Lopez, *et al.*, “Time-expanded Φ -OTDR using low-frequency electronics,” *Opt. Express* **31**(2), 843–852 (2023).
3. P. G. Hubbard, R. Ou, T. Xu, *et al.*, “Road deformation monitoring and event detection using asphalt-embedded distributed acoustic sensing (DAS),” *Struct. Control Health Monit.* **29**(11), e3067 (2022).
4. Z. W. Ding, X. P. Zhang, N. M. Zou, *et al.*, “Phi-OTDR based on-line monitoring of overhead power transmission line,” *J. Lightwave Technol.* **39**(15), 5163–5169 (2021).
5. X. Lu, K. Hicke, and K. Krebber, “Distributed acoustic sensing to monitor ground motion/movement at multi-frequency bands,” *J. Lightwave Technol.* **42**(18), 6269–6276 (2024).
6. E. F. Williams, M. R. Fernández-Ruiz, R. Magalhaes, *et al.*, “Distributed sensing of microseisms and teleseisms with submarine dark fibers,” *Nat. Commun.* **10**(1), 5778 (2019).
7. R. A. Rørstadbotnen, J. Eidsvik, L. Bouffaut, *et al.*, “Simultaneous tracking of multiple whales using two fiber-optic cables in the Arctic,” *Front. Mar. Sci.* **10**, 1130898 (2023).
8. P. J. Vidal-Moreno, C. Becerril, M. R. Fernández-Ruiz, *et al.*, “Noise analysis in direct detection and coherent detection phase-sensitive optical time-domain reflectometry systems,” *Opt. Express* **31**(17), 27450–27461 (2023).
9. F. Jiang, Z. Lu, F. Cai, *et al.*, “Low computational cost distributed acoustic sensing using analog I/Q demodulation,” *Sensors* **19**(17), 3753 (2019).
10. X. Hui, S. Zheng, J. Zhou, *et al.*, “Hilbert–Huang transform time-frequency analysis in Φ -OTDR distributed sensor,” *IEEE Photonics Technol. Lett.* **26**(23), 2403–2406 (2014).
11. Y. Li, Y. Wang, L. Xiao, *et al.*, “Phase demodulation methods for optical fiber vibration sensing system: A review,” *IEEE Sens. J.* **22**(3), 1842–1866 (2022).
12. D. B. Chester, “Digital IF filter technology for 3 G systems: An introduction,” *IEEE Commun. Mag.* **37**(2), 102–107 (1999).
13. Z. Chi, N. Zou, J. Shi, *et al.*, “Digital signal processing and application of Φ -OTDR system,” *Opto-Electron. Eng.* **50**(2), 220088-1 (2023).
14. S. Banerjee, Principles of Communication Engineering (2013).
15. N. A. Olsson, “Lightwave systems with optical amplifiers,” *J. Lightwave Technol.* **7**(7), 1071–1082 (1989).
16. X. Chen, N. Zou, Y. Wan, *et al.*, “On-line status monitoring and surrounding environment perception of an underwater cable based on the phase-locked Φ -OTDR sensing system,” *Opt. Express* **30**(17), 30312–30330 (2022).
17. M. Zabihi, Y. Chen, T. Zhou, *et al.*, “Continuous fading suppression method for Φ -OTDR systems using optimum tracking over multiple probe frequencies,” *J. Lightwave Technol.* **37**(14), 3602–3610 (2019).
18. J. R. Carson, “Notes on the theory of modulation,” *Proc. IEEE* **10**(1), 57–64 (1922).
19. S. Lin, Z. Wang, J. Xiong, *et al.*, “Rayleigh fading suppression in one-dimensional optical scatters,” *IEEE Access* **7**, 17125–17132 (2019).
20. Y. Koyamada, M. Imahama, M. Kubota, *et al.*, “Fiber-optic distributed strain and temperature sensing with very high measuring resolution over long range using coherent OTDR,” *J. Lightwave Technol.* **27**(9), 1142–1146 (2009).
21. L. Zhao, X. Zhang, and Z. Xu, “A high-fidelity numerical model of coherent Φ -OTDR,” *Measurement* **230**, 114526 (2024).
22. Y. Liu, H. Liu, X. G. Xia, *et al.*, “Projection techniques for altitude estimation over complex multipath condition-based VHF radar,” *IEEE J. Sel. Top. Appl. Earth Obs. Remote Sens.* **11**(7), 2362–2375 (2018).
23. X. Bao, D. P. Zhou, C. Baker, *et al.*, “Recent development in the distributed fiber optic acoustic and ultrasonic detection,” *J. Lightwave Technol.* **35**(16), 3256–3267 (2017).
24. J. C. Juarez, E. W. Maier, K. N. Choi, *et al.*, “Distributed fiber-optic intrusion sensor system,” *J. Lightwave Technol.* **23**(6), 2081–2087 (2005).
25. A. Masoudi and T. P. Newson, “Analysis of distributed optical fibre acoustic sensors through numerical modeling,” *Opt. Express* **25**(25), 32021–32040 (2017).

26. Y. Shan, W. Ji, Q. Wang, *et al.*, "Performance optimization for phase-sensitive OTDR sensing system based on multi-spatial resolution analysis," *Sensors* **19**(1), 83 (2019).
27. X. Lu and P. J. Thomas, "Numerical modeling of Fcy OTDR sensing using a refractive index perturbation approach," *J. Lightwave Technol.* **38**(4), 974–980 (2020).
28. Z. Ding, S. Wang, J. Kang, *et al.*, "Distributed acoustic sensing-based weight measurement method," *J. Lightwave Technol.* **42**(9), 3454–3460 (2024).
29. T. Dean, T. Cuny, and A. H. Hartog, "The effect of gauge length on axially incident P-waves measured using fibre optic distributed vibration sensing," *Geophys. Prospect.* **65**(1), 184–193 (2017).
30. S. Kang, D. E. Day, and J. O. Stoffer, "Measurement of the refractive index of glass fibers by the Christiansen-Shelyubskii method," *J. Non-Cryst. Solids* **220**(2-3), 299–308 (1997).
31. L. B. Liokumovich, N. A. Ushakov, O. I. Kotov, *et al.*, "Fundamentals of optical fiber sensing schemes based on coherent optical time domain reflectometry: Signal model under static fiber conditions," *J. Lightwave Technol.* **33**(17), 3660–3671 (2015).
32. K. Shimizu, T. Horiguchi, and Y. Koyamada, "Characteristics and reduction of coherent fading noise in Rayleigh backscattering measurement for optical fibers and components," *J. Lightwave Technol.* **10**(7), 982–987 (1992).
33. R. G. Priest, "Analysis of fiber interferometer utilizing 3×3 fiber coupler," *IEEE Trans. Microw. Theory Tech.* **30**(10), 1589–1591 (1982).
34. S. Alexander, "Design of wide-band optical heterodyne balanced mixer receivers," *J. Lightwave Technol.* **5**(4), 523–537 (1987).
35. Z. Xiao, J. Chen, J. Ji, *et al.*, "Complete phase noise compensation for 50 km DAS with 100 kHz linewidth ITLA," *Opt. Fiber Sens.* **F2.1**, F2.1 (2023).
36. Z. Ding, N. Zou, C. Zhang, *et al.*, "Self-optimized vibration localization based on distributed acoustic sensing and existing underground optical cables," *J. Lightwave Technol.* **40**(3), 844–854 (2022).
37. X. Zhang, L. Cao, Y. Shan, *et al.*, "Performance optimization for a phase-sensitive optical time-domain reflectometry based on multiscale matched filtering," *Opt. Eng.* **58**(05), 1–056114 (2019).
38. X. Zhang, Y. Zhang, F. Wang, *et al.*, "The mechanism and suppression methods of optical background noise in phase-sensitive optical time domain reflectometry," *Acta Phys. Sin.* **66**(7), 070707 (2017).
39. I. Bárány and V. Vu, "Central limit theorems for Gaussian polytopes," *Ann. Probab.* **35**(4), 1593–1621 (2007).
40. X Lu, M A Soto, and L. Thévenaz, "Optimal detection bandwidth for phase-sensitive optical time-domain reflectometry," *Sixth European Workshop on Optical Fibre Sensors* 9916, SPIE (2016).
41. S. I. Furukawa, Y. Koyamada, I. Sankawa, *et al.*, "Enhancement of OTDR performance with an optical fiber amplifier," *Electron. Comm. Jpn. Pt. I* **75**(12), 76–86 (1992).
42. A. V. Oppenheim, "Discrete-time signal processing," Pearson Education India (1999).